中国激光

基于超表面的阵列光场纵向维度信息编解码

樊鑫豪，武炫光，周亮，刘圣，赵建林，李鹏*

光场调控和信息感知工业和信息化部重点实验室，陕西省光信息技术重点实验室，西北工业大学物理科学与技术学院，陕西 西安 710129

摘要 随着大数据时代的到来，空间光通信已被广泛应用于各种通信系统中，但随之而来的是容量瓶颈的挑战。基于光场频率、时间、偏振、横向空间模式等维度调控的信息编解码方法在解决容量问题方面展现了优异性能，但光场的纵向维度却未被应用于信息编解码。针对此问题，本文提出了一种基于电介质超表面的光场纵向维度信息编解码新方法，基于四原子结构的几何相位和传输相位联合调控，实现了透射场自旋相关的复振幅调控。同时，利用光学冻结波原理产生了轨道角动量模式叠加态的纵向可控变化，并验证了光场模态的纵向调控能够以指数级提升信道中的模态容量。纵向维度作为一个全新的编码自由度，有望进一步提高自由空间光通信性能。

关键词 表面光学；超表面；纵向调控；复振幅；编码

中图分类号 O436 **文献标志码** A **DOI**：10.3788/CJL230727

1 引 言

自由空间光通信是一种以激光为信息载体的无线通信技术，具有通信容量大、速率高、安全性好等优点，是发展高速空间通信不可或缺的工具，已被广泛应用于各种通信系统中，如卫星被动光学遥感、激光雷达、微波光子雷达等[1-8]。光场携带着丰富的参量信息，如振幅、频率、时间、偏振等，围绕这些参量维度的调控，人们相继开发了一系列提升光通信容量的新技术[9-10]。但近年来，随着这些传统维度资源的开发殆尽，以及大数据时代的来临，光通信又一次面临着容量危机的挑战。为此，光场的空间结构（模态）逐渐被开发，用以解决日益严重的容量瓶颈问题。例如，携带有轨道角动量（OAM）的涡旋光束等，其空间模态能够构成高维Hilbert空间，可作为一种全新的编解码自由度，成为光通信持续扩容的重要突破口。

早在2004年，Gibson等[11]就提出了使用光束的OAM模态来编码信息的思想。借助OAM模态编解码可以有效提高自由空间光通信的安全性。2014年，Zeilinger研究小组[12]利用OAM模式叠加实现了长达3 km的自由空间编解码通信。进一步，该小组利用OAM模式叠加方法实现了143 km的自由空间编解码通信[13]。2015年，王健课题组[14]利用贝塞尔光束实现了自由空间多进制编解码通信。为了进一步实现光通信系统的扩容，该课题组又提出了产生随时间变化的空间阵列OAM模式，该模式可以有效提高自由空间光通信系统的信息容量[15]。2019年，高春清课题组[16]提出了一个发射端同时对应多个用户端的自由空间光通信系统，实现了一对四的同时通信。2020年，谢国强课题组[17]提出了一种多涡旋激光器，在自由空间实现了时间和空间上的信息编解码传输。2021年，陆延青课题组[18]基于电介质超表面实现了宽带广义完美庞加莱光束的产生，并将其应用于光信息的加解密中，有效提高了传输信息的安全性。2022年，申艺杰课题组[19]提出了一种三自由度多涡旋几何光束（MVGBs，其中三自由度指中心处OAM、子光束OAM、相干态相位），它可显著增强发散简并性，并且多个自由度在作为信息传输信道时相互独立且正交。

研究人员在充分探索OAM模式角向阶数复用的基础上，逐渐将径向阶数用于信息容量的进一步提升，如Boyd研究团队[20]利用偏振以及OAM模态的角向、径向量子数这三个横向自由度实现了8维量子密钥分发。此外，2015年，王健课题组[21]论证了矢量模式进行信息编解码的原理和能力，并采用16个矢量模式实现了64 pixel×64 pixel灰度图像的传输。随后，二维调控的矢量模态也逐渐被用于提升信息传输容量[22-24]。

尽管通过光场横向调控所得的空间模态已经充分证明了其在经典和量子通信中的可行性，然而到目前

收稿日期：2023-04-17；**修回日期**：2023-06-02；**录用日期**：2023-06-13；**网络首发日期**：2023-06-26

基金项目：国家重点研发计划（2022YFA1404800）、国家自然科学基金（12174309，12074312，12074313）、博士论文创新基金（CX2022076）

通信作者：*pengli@nwpu.edu.cn

为止，光场的另一个重要空间维度，即光场的纵向维度，在信息编解码过程中还未被应用。鉴于此，笔者提出了一种用于OAM模式叠加态纵向调控的电介质超表面。该超表面基于四原子结构的几何相位和传输相位能够实现透射场自旋相关的复振幅调控，进而产生0～15阶OAM模式叠加态的纵向变化。这种纵向变化的横向模式被应用到信息编码后，在单一信道中实现了模态容量为16^3的编解码，说明其能够指数级提升信道中的模态容量。

2　基本原理

2.1　光场纵向维度编解码原理

光场纵向维度编解码原理如图1(a)所示。发射端Bob发出的信息被ASCII(American Standard Code for Information Interchange)码编译为多个OAM模式叠加态，该叠加态由两个拓扑荷分别为l_1和l_2的OAM模式叠加而成，光斑呈现出$|l_1-l_2|$个“花瓣”形状。这些OAM叠加态被加载到模态纵向变化的光束阵列中进行空间传输，接收端Alice获取信息时，可以通过测量z_1、z_2、z_3等不同传输平面的阵列光场模态，并通过正确的解码顺序等操作获得信息。图1(b)给出了对应ASCII码的编解码表，所用OAM模式的拓扑荷选取为－8～8，叠加态呈现出16种不同的“花瓣”状强度模式。当光场引入纵向维度调控时，这种OAM模式叠加态沿纵向可以实现16种模态的任意变化(可以看作是一个16进制码元)，当模态纵向变化数目为m时，这个信道中加载的模态数目可增加到16^m。结合空间阵列结构，所提方案可以实现多信道并行传输，从而提升信息传输容量。

采用光学冻结波原理[25-28]实现OAM模态的纵向变化。假设具有特定纵向强度分布的冻结波是由$2N+1$个l阶贝塞尔光束同轴叠加而成的，则其电场分布可以写成

$$F_l(r,\phi,z)=\exp(-\mathrm{i}\omega t)\sum_{j=-N}^{N}A_j\mathrm{J}_l(k_{jr}r)\cdot\exp(\mathrm{i}k_{jz}z)\exp(\mathrm{i}l\phi),\tag{1}$$

式中：ω为角频率；J_l为l阶第一类贝塞尔函数；k_{jr}为横向波数，$k_{jr}=k^2-(k_{jz})^2$，其中$k=2\pi/\lambda$，k为波数；k_{jz}为纵向波数，$k_{jz}=Q+2\pi\mathrm{j}/L$，其中$Q$是一个与贝塞尔光束中心光斑半径有关的初始参数，$L$是纵向强度调制的有效范围；$A_j$为每个贝塞尔光束对应的权重因子，其大小由纵向强度包络函数$F(z)$决定，即

$$A_j=\frac{1}{L}\int_0^L F(z)\exp(-\mathrm{i}k_{jz}z)\mathrm{d}z。\tag{2}$$

计算过程中，选取$Q=0.9968k$，$N=6$，$L=1.2$ mm。当两个具有不同OAM模式的冻结波同轴叠加时，叠加态表示为

$$F_{l_1,l_2}(r,\phi,z)=\exp(-\mathrm{i}\omega t)\left[\sum_{j=-N}^{N}A_j\mathrm{J}_{l_1}(k_{jr}r)\exp(\mathrm{i}k_{jz}z)\exp(\mathrm{i}l_1\phi)+\sum_{j=-N}^{N}A_j\mathrm{J}_{l_2}(k_{jr}r)\exp(\mathrm{i}k_{jz}z)\exp(\mathrm{i}l_2\phi)\right]。\tag{3}$$

以图1(a)为例，发射端Bob以ASCII码16进制码元编码信息“N”“P”“U”时，产生的叠加态阶数(定义为“花瓣”数目)分别为4和14、5和0、5和5。对于这种情况，将信息编码到两个冻结波中进行传输，则每个冻结波的模态在纵向上变化三次。因此，两个光束在纵向依次呈现出阶数为4和14、5和0、5和5的OAM叠加态。

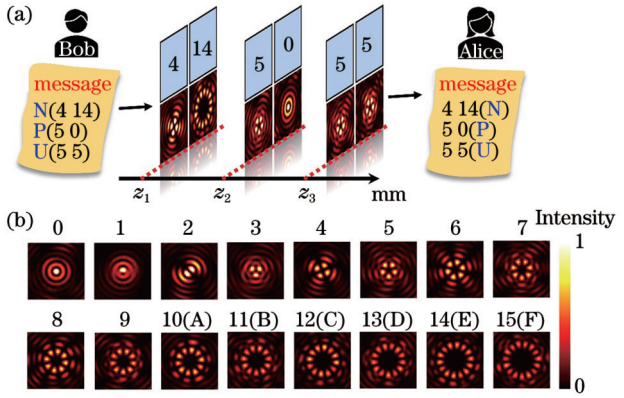

图1　纵向维度编解码的基本原理。(a)发射端Bob以ASCII码16进制码元编码信息“N”“P”“U”到两个并行传输的光束中，其在不同传输距离处分别呈现角向阶数为4和14、5和0、5和5的OAM模式叠加态，接收端Alice通过测量这些光束在z_1、z_2、z_3平面处的阶数来解码信息；(b)具有不同角向阶数的OAM模式叠加态的归一化强度分布及其所对应的ASCII码16进制码元

Fig. 1　Longitudinally encoding and decoding principles. (a) According to the ASCII hexadecimal encode, at the transmitter side, Bob encodes the message “N”, “P”, “U” into two beams, which orderly present distinct superposition states of OAM modes with azimuthal orders of 4 and 14, 5 and 0, 5 and 5 at different propagation distances. At the receiver side, Alice decodes the message by measuring these beams orders at z_1, z_2, and z_3 planes. (b) Normalized intensity distributions of superposition states of OAM modes with different azimuthal orders and the corresponding ASCII hexadecimal code elements

2.2　超表面设计

采用上述原理产生模态纵向变化的光场时，通过对式(1)进行傅里叶变换，获得频谱面上的复振幅调制函数。根据贝塞尔函数的傅里叶变换特性，横向波矢分量不同的贝塞尔函数的频谱为半径不同的狄拉克(δ)环，其权重因子A_j保持不变，因而频谱面的复透过率可表示为

$$U_{F_l}(k_{rj}, z=0)=\sum_{j=-N}^{N} A_j \delta(k_r-k_{rj})\exp(\mathrm{i}l\phi)。\quad (4)$$

为了实现式(4)所示的复振幅调制，本文采用图 2(a)所示的四原子电介质超表面，其单元结构是沉积在透明衬底上的具有高折射率的旋转矩形纳米柱，纳米柱的几何参数分别由 P_0(周期)、H_0(高度)、L_0(长度)和 W_0(宽度)表示。高折射率纳米柱的光场调控可以用等效波导理论进行分析，该结构存在偏振方向平行于矩形结构长、短轴的两个本征模式，其透射场的振幅和相位与单元结构的几何参数密切相关。因此，该旋转矩形纳米柱结构可作为等效双折射元件进行波前调制。

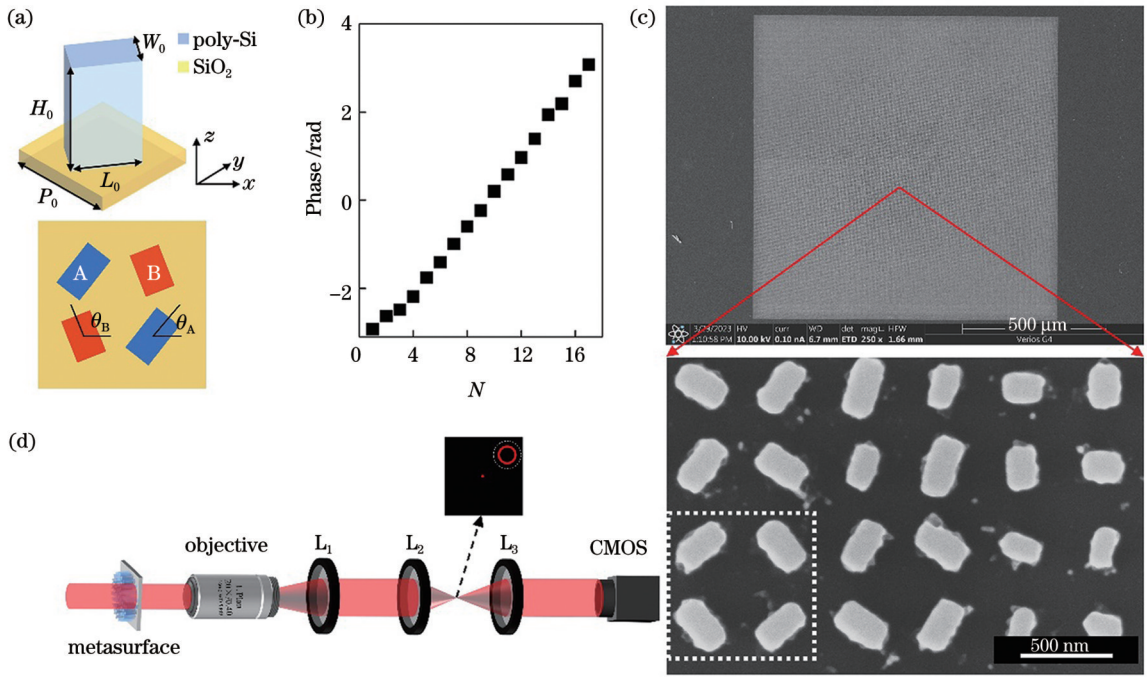

图 2　四原子宏像素多晶硅超表面及实验表征光路。(a)上图是沉积在 SiO_2 衬底上的多晶硅纳米柱单元结构示意图(几何参数为周期 P_0、高度 H_0、长度 L_0、宽度 W_0)，下图是四原子宏像素结构俯视图，其中 θ_A 和 θ_B 为矩形纳米柱相对于参考坐标系的旋转角度；(b)17 个选定的几何形状的传输相位；(c)超表面的扫描电子显微镜(SEM)图像及其局部放大图，白色虚线框内为四原子宏像素；(d)实验装置示意图(超表面放置在沿 z 方向运动的线性位移平台上)

Fig. 2　Tetratomic macro-pixel polycrystalline silicon metasurface and the experimental setup. (a) The upper image shows meta-atom of poly-Si nanopillar deposited on SiO_2 substrate with geometric parameters of P_0 (period), H_0 (height), L_0 (length), and W_0 (width), and lower image is the top view of the tetratomic macro-pixel structure, where θ_A and θ_B are the rotation angles of the rectangular nanopillars with respect to the reference coordinate system; (b) transmitted phases of 17 selected geometries; (c) SEM images of metasurface and its local area, and a tetratomic macro-pixel is exhibited in the dashed box; (d) experimental setup schematic (the metasurface is placed on a linear displacement stage that moves along the z-direction)

假设两偏振分量具有相同的透射振幅 T，则单元结构调制作用可以用琼斯矩阵表示为

$$\boldsymbol{J}=\boldsymbol{R}(-\theta)\begin{bmatrix} T\exp(\mathrm{i}\varphi_x) & 0 \\ 0 & T\exp(\mathrm{i}\varphi_y)\end{bmatrix}\boldsymbol{R}(\theta),\quad (5)$$

式中：$\boldsymbol{R}(\cdot)$ 是旋转矩阵；φ_x 和 φ_y 分别表示矩形结构长、短轴方向所对应偏振分量的相位延迟。为了引入几何相位调控，令 $\varphi_x-\varphi_y=\pi$。对于圆偏振入射光 $[1\ \mathrm{i}]^{\mathrm{T}}$，单元结构的输出场可以表示为

$$\boldsymbol{E}=T\exp\left[\mathrm{i}(\varphi_0-2\theta)\right]\begin{bmatrix}1\\-\mathrm{i}\end{bmatrix},\quad (6)$$

式中：φ_0 表示单元结构引入的传输相位，$\varphi_0=(\varphi_x+\varphi_y)/2$。由式(6)可以看出，圆偏振光入射相位延迟为 π 的单元结构后，透射场转变为相反的圆偏振态，同时仅产生传输相位和几何相位调制[表示为 $\exp(\mathrm{i}2\theta)$]作用。为了引入振幅调制，将相邻的单元结构排列成图 2(a)所示的四原子宏像素结构，通过相邻单元结构光学响应之间的内在关系与相互作用，引入偏振相关干涉实现复振幅调控。在四原子宏像素结构中，具有相同周期和高度的电介质单元结构以 2×2 的正方形晶格形式排布，对角线上的两个单元结构具有相同的几何参数和方位角，分别表示为单元结构 A 和单元结构 B。当入射光为线偏振光时，单元结构 A、B 都会产生相位调控作用，

$$\begin{cases}\boldsymbol{E}_{\mathrm{out}}^{\mathrm{A}}=\exp\left[\mathrm{i}(\varphi_{0\mathrm{A}}+2\theta_{\mathrm{A}})\right]|\boldsymbol{R}\rangle+\exp\left[\mathrm{i}(\varphi_{0\mathrm{A}}-2\theta_{\mathrm{A}})\right]|\boldsymbol{L}\rangle\\ \boldsymbol{E}_{\mathrm{out}}^{\mathrm{B}}=\exp\left[\mathrm{i}(\varphi_{0\mathrm{B}}+2\theta_{\mathrm{B}})\right]|\boldsymbol{R}\rangle+\exp\left[\mathrm{i}(\varphi_{0\mathrm{B}}-2\theta_{\mathrm{B}})\right]|\boldsymbol{L}\rangle\end{cases},\quad (7)$$

式中：$\boldsymbol{E}_{\mathrm{out}}^{\mathrm{A}}$ 和 $\boldsymbol{E}_{\mathrm{out}}^{\mathrm{B}}$ 分别表示经 A、B 单元结构调制后的输出光；$\varphi_{0\mathrm{A}}$ 和 $\varphi_{0\mathrm{B}}$ 分别表示单元结构 A 和 B 的传输相位；θ_{A} 和 θ_{B} 分别表示单元结构 A 和 B 的旋转角度；$|\boldsymbol{R}\rangle$

和|**L**〉分别表示右旋圆和左旋圆偏振单位矢量。此时，单元结构 A 和 B 可以视作不同的干涉源，所调制的光场中具有相同自旋态的分量将进行相干叠加，以构建最终的输出场，即

$$\begin{cases} E_{\text{out}}^{\text{R}} = \exp\left[\text{i}\left(\varphi_{0\text{A}} + 2\theta_{\text{A}}\right)\right] + \exp\left[\text{i}\left(\varphi_{0\text{B}} + 2\theta_{\text{B}}\right)\right] = 2\cos\left(\dfrac{\varphi_{0\text{A}} - \varphi_{0\text{B}}}{2} + \theta_{\text{A}} - \theta_{\text{B}}\right)\exp\left[\text{i}\left(\dfrac{\varphi_{0\text{A}} + \varphi_{0\text{B}}}{2} + \theta_{\text{A}} + \theta_{\text{B}}\right)\right] \\ E_{\text{out}}^{\text{L}} = \exp\left[\text{i}\left(\varphi_{0\text{A}} - 2\theta_{\text{A}}\right)\right] + \exp\left[\text{i}\left(\varphi_{0\text{B}} - 2\theta_{\text{B}}\right)\right] = 2\cos\left(\dfrac{\varphi_{0\text{A}} - \varphi_{0\text{B}}}{2} - \theta_{\text{A}} + \theta_{\text{B}}\right)\exp\left[\text{i}\left(\dfrac{\varphi_{0\text{A}} + \varphi_{0\text{B}}}{2} - \theta_{\text{A}} - \theta_{\text{B}}\right)\right] \end{cases}, \tag{8}$$

式中：$E_{\text{out}}^{\text{L}}$ 和 $E_{\text{out}}^{\text{R}}$ 分别表示输出场的左旋和右旋分量。显然，输出场中两个正交自旋分量具有独立的复振幅解析表达式。因此，利用四原子宏像素以及偏振相关干涉作用即可实现光场复振幅的调控。由式(8)可以看出左旋和右旋两个正交偏振信道中可以实现不同的复振幅调制，因此这种四原子超表面还可以实现偏振信道复用。在后续的实验过程中，仅对一个偏振信道中的光场模态进行实验表征。

根据这一原理，联立式(3)和式(8)可得到单元结构 A、B 的传输相位 $\varphi_{0\text{A}}$、$\varphi_{0\text{B}}$ 和旋转角 θ_{A}、θ_{B}。本次实验选择了多晶硅(折射率为 3.19+0.01i)和 SiO_2 分别作为高折射率材料和衬底，选用波长为 632.8 nm 的光源，在高度 H_0=590 nm、周期 P_0=400 nm 的条件下扫描不同长(L_0)和宽(W_0)的纳米柱的透射场，找出 17 种不同的几何形状，使其传输相位 φ_0 满足图 2(b)所示的线性变化关系。

3　实验结果与讨论

根据上述理论，采用电子束曝光和等离子体刻蚀的方法制备超表面[29-30]。图 2(c)显示了超表面的扫描电子显微镜(SEM)图像及其局部放大图。如局部放大图所示，四原子宏像素纳米柱周期为 800 nm，对角结构具有相同的尺寸和旋向，超表面的像素为 1250×1250。图 2(d)为实验装置示意图，来自 He-Ne 激光器的波长为 632.8 nm 的线偏振光束入射到超表面，在其后产生携带有编码信息的纵向分段阵列光场。采用放大倍数为 20 的物镜(NA 为 0.4)、准直透镜 L_1(f_1=10 cm)、4f 系统透镜 L_2(f_2=15 cm)、准直透镜 L_3(f_3=15 cm)以及 CMOS 相机组成的显微测量系统来表征光场。该相机的分辨率为 2048×2048，像元大小为 5.5 μm×5.5 μm(acA2040，Basler)。实验中，超表面固定在线性位移平台上，用以实现不同纵向位置处光场强度的测量。为了避免直透光对实验现象造成干扰，使用 4f 滤波系统滤除直透光。在实验中，将超表面的后表面设置为 z=0 平面。

为了证明这种特殊光场的纵向维度编码能力，实验中所用的编码信息为“Northwestern Polytechnical University”，使用 ASCII 码 16 进制码元对每个单词中的每一个字母以及单词与单词之间的空格进行编码，每一个字母对应两个 16 进制数字，因此编码完整信息需要 74 个模态来实现光束角向阶数与编码信息的一一对应。所以，实验中采用 5×5 的阵列光束，并将每束冻结波的纵向调制范围 L 分为三段，分别对应 0～0.4 mm，>0.4～0.8 mm，>0.8～1.2 mm。在单个冻结波信道中，由于纵向分为三段调制，每段均有 16 种可用模态，因此单个信道中可传输编码的模态总容量为 16^3。本实验所采用的冻结波是准无衍射光束，而且这 25 束光同时传输、相互独立，两两光束之间紧邻，每一束光代表一个信道，在无衍射距离内的任一段传输距离处产生的 25 幅衍射图样均可单次采集并可同时获得。为了清晰地辨别每束光的角向阶数信息并顺利完成信息解码工作，只留下了中心处的强度分布，如图 3 所示。舍去第 25 束冻结波的第三段，用剩余冻结波完成对应信息的编码。在 z_1=0.1 mm、z_2=0.5 mm 和 z_3=0.9 mm 处的模拟结果如图 3(a)所示，图中 m 表示阵列光束的行数，n 表示列数，光场强度图左上角的数字表示角向阶数信息。

实验结果如图 3(b)所示，展示了 z_1=0.1 mm、z_2=0.5 mm 和 z_3=0.9 mm 平面上测量的光场强度分布。如图 3 所示，实验测量结果与数值模拟结果相吻合，阵列光束均呈现出按需变化的 OAM 模式叠加态。在 z_1 处，从第一行开始按“Z”字形顺序，两个 16 进制数字为一组进行解码，得到了所传递的信息“Northwestern Polytechnical University”。需要说明的是，实验中光场的纵向模态变化数目仅为 3，而采用所提方法可以实现更高次的纵向调控，因此这种信道容量增长的指数因子还可进一步增大。但是，在解码时，需要对三个不同平面的光场模态进行测量，而本文采用了纵向扫描的方法。为了提高解码效率，还可以采用分平面成像的办法，通过两次分光，然后再对不同纵向平面进行成像，一次获取三个纵向平面的光场分布。此外，根据光波的传播特性，如果在单一平面上测得了光场的复振幅信息，就可以通过数值计算的方法获取其他平面的复振幅分布，进而得到多个纵向平面的光场模式[31]。

4　结　　论

本文提出了一种光场偏振态和复振幅独立控制的电介质超表面，在完全控制光场复振幅的基础上，通过冻结波的频谱调控原理实现了阵列冻结波纵向维度上

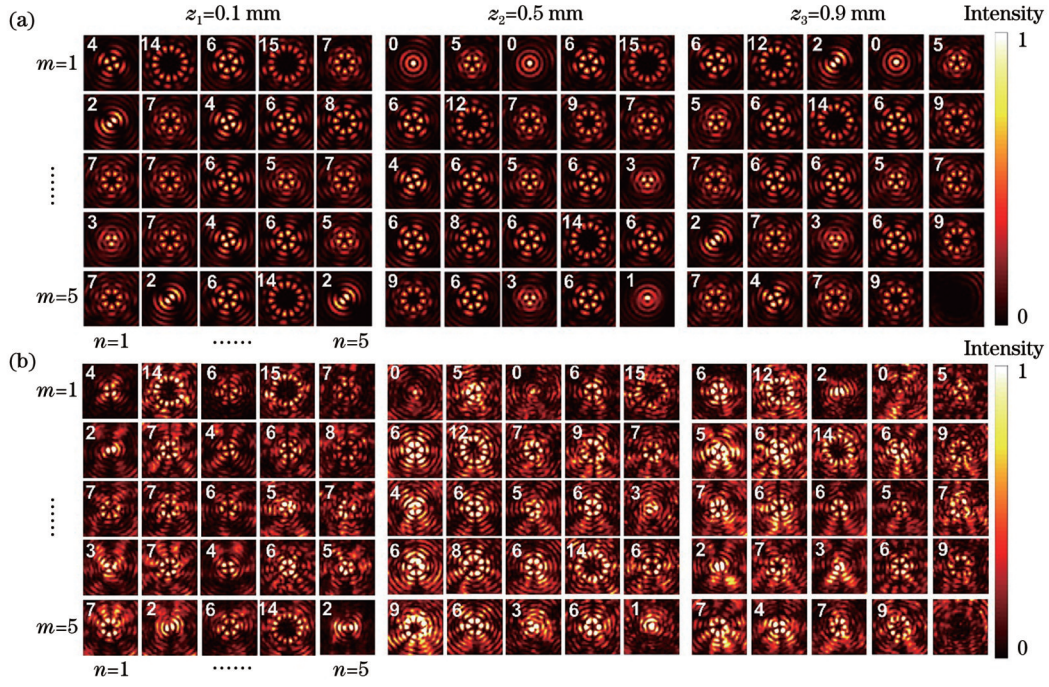

图 3　模拟和测量的编码“Northwestern Polytechnical University”信息所产生的纵向调控光场阵列在 z_1=0.1 mm、z_2=0.5 mm、z_3=0.9 mm 平面上的强度分布及其角向阶数信息(左上角),其中 m 和 n 分别表示阵列光束的行数和列数。(a)模拟结果;(b)测量结果

Fig. 3　Simulated and measured intensity distributions and azimuthal orders (top left) of longitudinally modulated beam array encoded with message “Northwestern Polytechnical University” in the planes of z_1=0.1 mm, z_2=0.5 mm, and z_3=0.9 mm, where the symbols m and n denote row and column numbers of the beam array, respectively. (a) Simulated results; (b) measured results

OAM 模式叠加态的灵活调控。利用这些模态纵向变化的光场,通过实验实现了幂指数级的信道模态扩容,有效提升了信道中的模态容量。本文所验证的纵向维度编解码功能有望成为自由空间光通信容量增加的新突破口。

参　考　文　献

[1] Wang Y, Wu C C. Current understanding of tropical cyclone structure and intensity changes-a review[J]. Meteorology and Atmospheric Physics, 2004, 87(4): 257-278.

[2] Kim D, Ramanathan V. Solar radiation budget and radiative forcing due to aerosols and clouds[J]. Journal of Geophysical Research, 2008, 113(D2): D02203.

[3] Jamet C, Ibrahim A, Ahmad Z, et al. Going beyond standard ocean color observations: lidar and polarimetry[J]. Frontiers in Marine Science, 2019, 6: 251.

[4] 龚威, 史硕, 陈博文, 等. 机载高光谱激光雷达成像技术发展与应用[J]. 光学学报, 2022, 42(12): 1200002.
Gong W, Shi S, Chen B W, et al. Development and application of airborne hyperspectral LiDAR imaging technology[J]. Acta Optica Sinica, 2022, 42(12): 1200002.

[5] Li R M, Li W Z, Ding M L, et al. Demonstration of a microwave photonic synthetic aperture radar based on photonic-assisted signal generation and stretch processing[J]. Optics Express, 2017, 25(13): 14334-14340.

[6] Wang A L, Zheng D K, Du S R, et al. Microwave photonic radar system with ultra-flexible frequency-domain tunability[J]. Optics Express, 2021, 29(9): 13887-13898.

[7] Zhang F Z, Guo Q S, Zhang Y, et al. Photonics-based real-time and high-resolution ISAR imaging of non-cooperative target[J]. Chinese Optics Letters, 2017, 15(11): 112801.

[8] Zhang F Z, Guo Q S, Wang Z Q, et al. Photonics-based broadband radar for high-resolution and real-time inverse synthetic aperture imaging[J]. Optics Express, 2017, 25(14): 16274-16281.

[9] Zhou X, Yu J J. Multi-level, multi-dimensional coding for high-speed and high-spectral-efficiency optical transmission[J]. Journal of Lightwave Technology, 2009, 27(16): 3641-3653.

[10] Winzer P J, Gnauck A H, Doerr C R, et al. Spectrally efficient long-haul optical networking using 112-Gb/s polarization-multiplexed 16-QAM[J]. Journal of Lightwave Technology, 2010, 28(4): 547-556.

[11] Gibson G, Courtial J, Padgett M J, et al. Free-space information transfer using light beams carrying orbital angular momentum[J]. Optics Express, 2004, 12(22): 5448-5456.

[12] Krenn M, Fickler R, Fink M, et al. Communication with spatially modulated light through turbulent air across Vienna[J]. New Journal of Physics, 2014, 16(11): 113028.

[13] Krenn M, Handsteiner J, Fink M, et al. Twisted light transmission over 143 km[J]. Proceedings of the National Academy of Sciences of the United States of America, 2016, 113(48): 13648-13653.

[14] Du J, Wang J. High-dimensional structured light coding/decoding for free-space optical communications free of obstructions[J]. Optics Letters, 2015, 40(21): 4827-4830.

[15] Li S H, Wang J. Experimental demonstration of optical interconnects exploiting orbital angular momentum array[J]. Optics Express, 2017, 25(18): 21537-21547.

[16] Fu S Y, Zhai Y W, Zhou H, et al. Demonstration of free-space one-to-many multicasting link from orbital angular momentum encoding[J]. Optics Letters, 2019, 44(19): 4753-4756.

[17] Qiao Z, Wan Z Y, Xie G Q, et al. Multi-vortex laser enabling spatial and temporal encoding[J]. PhotoniX, 2020, 1(1): 1-14.

[18] Liu M Z, Huo P C, Zhu W Q, et al. Broadband generation of perfect Poincaré beams via dielectric spin-multiplexed metasurface [J]. Nature Communications, 2021, 12: 2230.

[19] Wan Z S, Shen Y J, Wang Z Y, et al. Divergence-degenerate spatial multiplexing towards future ultrahigh capacity, low error-

rate optical communications[J]. Light: Science & Applications, 2022, 11: 144.
[20] Zhou Y Y, Mirhosseini M, Oliver S, et al. Using all transverse degrees of freedom in quantum communications based on a generic mode sorter[J]. Optics Express, 2019, 27(7): 10383-10394.
[21] Zhao Y F, Wang J. High-base vector beam encoding/decoding for visible-light communications[J]. Optics Letters, 2015, 40(21): 4843-4846.
[22] Zhu Z Y, Janasik M, Fyffe A, et al. Compensation-free high-dimensional free-space optical communication using turbulence-resilient vector beams[J]. Nature Communications, 2021, 12: 1666.
[23] Chen W H, He H X, Lin Q A, et al. Meta-learning-based optical vector beam high-fidelity communication under high scattering[J]. Optics Letters, 2022, 47(12): 3131-3134.
[24] Xian M C, Xu Y, Ouyang X, et al. Segmented cylindrical vector beams for massively-encoded optical data storage[J]. Science Bulletin, 2020, 65(24): 2072-2079.
[25] Zamboni-Rached M. Stationary optical wave fields with arbitrary longitudinal shape by superposing equal frequency Bessel beams: frozen waves[J]. Optics Express, 2004, 12(17): 4001-4006.
[26] Vieira T A, Gesualdi M R R, Zamboni-Rached M. Frozen waves: experimental generation[J]. Optics Letters, 2012, 37(11): 2034-2036.
[27] Vieira T A, Gesualdi M R R, Zamboni-Rached M, et al. Production of dynamic frozen waves: controlling shape, location (and speed) of diffraction-resistant beams[J]. Optics Letters, 2015, 40(24): 5834-5837.
[28] Li P, Wu D J, Zhang Y, et al. Polarization oscillating beams constructed by copropagating optical frozen waves[J]. Photonics Research, 2018, 6(7): 756-761.
[29] Guo X Y, Zhong J Z, Li B J, et al. Full-color holographic display and encryption with full-polarization degree of freedom[J]. Advanced Materials, 2022, 34(3): 2103192.
[30] Guo X Y, Li P, Zhong J Z, et al. Stokes meta-hologram toward optical cryptography[J]. Nature Communications, 2022, 13: 6687.
[31] Zhong J Z, Liu S, Guo X Y, et al. Reconstructing the topology of optical vortex lines with single-shot measurement[J]. Applied Physics Letters, 2021, 119(16): 161102.

Longitudinally Encoding and Decoding Information in Light Field Arrays Based on Metasurface

Fan Xinhao, Wu Xuanguang, Zhou Liang, Liu Sheng, Zhao Jianlin, Li Peng*

Key Laboratory of Light Field Manipulation and Information Acquisition, Ministry of Industry and Information Technology, Shaanxi Province Key Laboratory of Optical Information Technology, School of Physical Science and Technology, Northwestern Polytechnical University, Xi'an 710129, *Shaanxi, China*

Abstract

Objective Free-space optical communication, which uses a laser as an information carrier, is a wireless communication technology that is widely used in various communication systems. Owing to sufficient parametric dimensions, a series of new technologies have been developed to enhance optical communication capacity based on light field modulation. However, in recent years, with the exhaustion of these traditional dimensional resources and the advent of the "big data" era, optical communication is once again facing the challenge of a capacity crisis. In response, spatial structures (modes) of light fields are gradually being developed to address the growing capacity bottlenecks. For example, vortex beams carrying orbital angular momentum (OAM) have become an important breakthrough for sustainable capacity expansion of optical communications because their spatial modes are a new degree of freedom in constructing a high-dimensional Hilbert space. Consequently, various methods have emerged to encode information using the azimuthal order of OAM modes. Besides the azimuthal order multiplexing of OAM modes, the radial index and the vector modes are also used to achieve further information capacity enhancement. Although the spatial modes obtained based on the transverse modulation of light fields have fully demonstrated their feasibility in classical and quantum communications, another important spatial dimension of the light field, that is, the longitudinal dimension, has not been exploited for information encoding and decoding. Herein, we propose a dielectric metasurface for longitudinally modulating the superposition state of OAM modes and demonstrate the capability of these modulated light fields in information-encoding scenarios. The metasurface consists of tetratomic macropixels, which enable spin-dependent complex amplitude modulation of the transmitted field because of polarization-dependent interference and can produce a 5×5 light beam array with each beam channel presenting longitudinally variant superposition states of 0 to 15 orders. By introducing longitudinal modulation, the mode capacity of individual channels can be increased exponentially, depending on the number of longitudinal segments in the superposition state of the OAM modes.

Methods The longitudinal encoding and decoding principles are shown in Fig. 1(a). The information from Bob at the transmitter is compiled into multiple superposition states composed of two OAM modes with topological charges of l_1 and l_2 according to the American Standard Code for Information Interchange (ASCII). As the superposition state presents the intensity distribution as the shape of $|l_1-l_2|$ "petals", it is characterized by the azimuthal order $|l_1-l_2|$. These superposition states are then loaded into light beams with longitudinal on-demand transformations for spatial transmission. Alice at the receiver side can obtain the correct information by measuring the superposition modes in different transmission planes, such as z_1, z_2, and z_3, and by decoding the correct sequence of operations. Figure 1(b) shows the codec table corresponding to the ASCII codes and the superposition states with azimuthal orders varying from 0 to 15. Moreover, a spatial array structure can be introduced to increase the parallel transmission rate of information.

An optical frozen wave was used to realize the longitudinal modulation of the OAM modes, and a tetratomic macro-pixel dielectric metasurface was designed to experimentally generate such a light field array with encoded information. The tetratomic macro-pixel is shown in Fig. 2(a), which considers the intrinsic relationship and interaction between the optical responses of rectangular meta-atoms and can achieve complex amplitude modulation because of polarization-dependent interference. According to this principle, the transmission phases φ_{0A} and φ_{0B} and rotation angles θ_A and θ_B of the meta-atoms A and B in a tetratomic pixel can be obtained by combining equations (3) and (8). The transmission fields of rectangular nanopillars with different lengths and widths were scanned under the conditions of height H_0=590 nm and period P_0=400 nm to find 17 different geometries, of which the transmitted phases φ_0 linearly increased as shown in Fig. 2(b).

Results and Discussions As an example, the message "Northwestern Polytechnical University" is used to demonstrate the longitudinally encoding capability of this specially structured light field. According to the ASCII hexadecimal code elements, the letters and spaces in the message are transformed into 74 superposition states, which are then divided into a 5×5 beam array. The longitudinal variation of each beam channel contains three segments, which are located at propagation distances of z=0–0.4 mm, 0.4–0.8 mm, and 0.8–1.2 mm, respectively. Because the superposition state in each beam channel can change three times along the longitudinal dimension, the total mode capacity of the beam array is expanded to 16^3. The simulated and measured intensity distributions of beam arrays in z_1=0.1 mm, z_2=0.5 mm, and z_3=0.9 mm planes are shown in Fig. 3. The experimental measurements are consistent with that of the simulations. Therefore, the correct message can be obtained by decoding two hexadecimal digits in a Z-shaped sequence starting from the first line in z_1. It should be noted that this method requires the measurement of the light field modes in three different planes for decoding. In this study, a longitudinal scanning method is used. However, to improve the decoding efficiency, a split-plane imaging approach can also be used to obtain the light-field distribution in three longitudinal planes simultaneously by splitting the light twice and then imaging different longitudinal planes. In addition, according to the propagation characteristics of light waves, if the complex amplitude information of the light field is measured in a single plane, the complex amplitude distributions of other planes can be obtained by numerical calculations, and the light field patterns of multiple longitudinal planes can then be obtained.

Conclusions In this study, a dielectric metasurface that can independently control the amplitude and phase of two light fields is proposed. Flexible modulation of the OAM modes of the beam array in the longitudinal dimension is achieved using the spectral modulation principle of frozen waves. Using these longitudinally modulated light fields, exponential expansion of the mode capacity is experimentally realized to enhance the mode capacity of free-space optical communication. The longitudinal dimensional coding and decoding functionality verified in this study is expected to be a breakthrough in the capacity improvement of free-space optical communication.

Key words optics at surface; metasurface; longitudinal modulation; complex amplitude; encoding